Water Resources Research

RESEARCH ARTICLE
10.1029/2021WR029717

The Effect of Roughness Spacing and Size on the Lateral Deflection of Bedload Particles

Chuanqi He[1,2,3], Ci-Jian Yang[2], and Jens M. Turowski[2]

[1]School of Earth Sciences, China University of Geosciences, Wuhan, China, [2]German Research Centre for Geosciences (GFZ), Potsdam, Germany, [3]School of Earth Sciences, Zhejiang University, Hangzhou, China

Key Points:

- For large roughness elements, the deflection length and velocity show a peak at intermediate values of roughness element spacing
- The probability of leaving the roughness zone decays with the distance from its edge
- Lateral erosion rate in bedrock rivers is affected by the position of the roughness zone and its relation to the particle path

Supporting Information:

Supporting Information may be found in the online version of this article.

Correspondence to:

J. M. Turowski,
jens.turowski@gfz-potsdam.de

Citation:

He, C., Yang, C.-J., & Turowski, J. M. (2021). The effect of roughness spacing and size on the lateral deflection of bedload particles. *Water Resources Research*, *57*, e2021WR029717. https://doi.org/10.1029/2021WR029717

Received 16 FEB 2021
Accepted 18 SEP 2021

Abstract Bedrock river lateral erosion plays a crucial role in landscape evolution, sediment transport and deposition, and the occurrence of geohazards. Fluvial erosion of massive rock is largely driven by impacts of bedload particles, which also drives crack propagation to prepare blocks for plucking. In straight channels, bedload particles generally move parallel to the channel walls and thus need to be deflected laterally to cause wall erosion. Sideward deflection of bedload particles occurs when they interact with roughness elements fixed on the riverbed. Here, we isolated the interaction of moving bedload particles with roughness elements in laboratory experiments. We conducted 21 sets of flume experiments to systematically investigate how spacing (5, 10, 20, 30, 40, 50, and 60 mm) and size (5, 10, and 20 mm) of roughness elements influence sideward deflection of bedload particles in straight channels with relatively low flow depth and a localized roughness zone covering half of the channel width. Velocity changes by the first impact increase with the size of roughness elements. The deflection length and velocity peak at intermediate values of the spacing of roughness elements. The likelihood for a bedload particle to leave the roughness zone decays with the bedload particle's distance to its edge. Our results suggest that lateral erosion rates in bedrock channels are dominantly controlled by the position of the roughness zone within the channel and its relation to the particle path.

Plain Language Summary Erosion of the bedrock walls of a river gorge is driven by the impact of sediment particles propelled by the water flow. Both water flow and sediment particles generally move in parallel to the walls, and the particles need to be deflected laterally from their downstream path to impact the walls. Sideward deflection occurs when the particles hit an obstacle on the river bed, such as a boulder. We investigate the sideward deflected length and velocity of moving particles in a laboratory flume experiment for various configurations of obstacles fixed to the bed. The spacing and size of obstacles have a dual control on deflected length and velocity, making deflection possible in the first case, but also limiting the free path until further impacts. Thus, there exists an optimal spacing of obstacles for maximizing sideward deflection length and velocity.

1. Introduction

Fluvial bedrock erosion is a key component in landscape evolution, and thus a crucial process in shaping the Earth's surface (e.g., Burbank et al., 1996; Cook et al., 2014; Scheingross et al., 2019; Turowski et al., 2013). Bedrock erosion can be divided into the vertical incision and lateral erosion. Vertical incision deepens the valleys, steepens the hillslopes, and is thus a primary process for landscapes to respond to spatial-temporal variations of tectonic deformation (e.g., He et al., 2019, 2021; Lamb & Fonstad, 2010; Larsen & Montgomery, 2012), rock resistance (e.g., Duvall et al., 2004; Sklar & Dietrich, 2001), and climate (e.g., Hartshorn et al., 2002; Murphy, et al., 2016). Compared to vertical incision, lateral erosion has received less attention (e.g., Finnegan, et al., 2014; Hartshorn et al., 2002). However, an understanding of lateral erosion is required to model important aspects of landscape evolution, including bedrock river response to tectonic and climatic conditions (e.g., Turowski, 2020), and controls on channel and valley width and shape (e.g., Fuller et al., 2016; Langston & Tucker, 2018; Li et al., 2021; Turowski, 2018; Turowski et al., 2008), sediment transport and deposition (e.g., Cook et al., 2020; Inoue et al., 2021; Mishra et al., 2018), hillslope stability (e.g., Malatesta et al., 2017), and sinuosity (e.g., Inoue et al., 2021; Shepherd, 1972; Turowski, 2018).

Particle impact is an efficient way to transfer energy and momentum from the flow to the bedrock (Sklar & Dietrich, 2004). Impacts by moving bedload particles play a crucial role in the two most common fluvial

bedrock erosion processes, abrasion and plucking. In the abrasion process, the erosion rate is assumed to be proportional to the energy delivered to the bedrock by the impacts of particles (Sklar & Dietrich, 2004). In the plucking process, individual blocks are removed by hydraulic processes from the bedrock. Here, bedload impacts drive crack propagation and therefore contribute to the preparation of blocks, a process known as macro-abrasion (Chatanantavet & Parker, 2009). Gilbert (1877) suggested that lateral erosion happens when the channel bed is covered by alluvial deposits, which inhibit vertical incision. Physical and numerical experiments indicate that an increase in bedload particle supply can accelerate lateral erosion (e.g., Finnegan et al., 2007; Inoue et al., 2021; Johnson & Whipple, 2010; Li et al., 2021; Mishra et al., 2018; Shepherd, 1972).

Rolling, sliding, and saltation are common modes of bedload transport in natural rivers. All of these modes can be expected to contribute to vertical and lateral erosion of bedrock channels. However, the relative importance of these transport modes to total erosion is currently unclear. Flume experiments indicate that rolling particles deliver more energy at low acoustic frequency, while saltating particles generate stronger responses at a high acoustic frequency (Tsakiris et al., 2014). Turowski et al. (2015) studied energy delivery to the channel bed by moving bedload particles in a natural stream and found that the largest particles deliver more energy than would be expected from a scaling just dependent on particle mass. They attributed the larger energy delivered per mass to be due to their higher probability of roll or slide (Auel et al., 2017). These transport modes deliver less energy per impact but impact the bed more frequently per unit travel distance (cf. Turowski & Rickenmann, 2009).

In straight channels, bedload particles generally move parallel to the channel walls. To cause lateral erosion of bedrock walls by impacts, bedload particles need to be sideward deflected and hit the riverbanks with sufficient energy to cause damage. Following the lead of Gilbert (1877), previous research has established the role of the interaction of moving bedload particles with roughness elements on the riverbed in setting lateral bedrock erosion (e.g., Beer et al., 2017; Finnegan et al., 2007; Fuller et al., 2016; Li et al., 2020, 2021; Mishra et al., 2018; Shepherd, 1972; Turowski, 2018). As bedload particles move downstream in fully alluviated channels, their cross-stream velocity fluctuates around zero due to sideward diffusion, with a symmetric exponential distribution (Fathel et al., 2015; Seizilles et al., 2014). In a series of experiments, Fuller et al. (2016) demonstrated that roughness elements fixed on the channel bed show a dominant control on lateral bedrock erosion, a notion that is supported by field observations in a bedrock gorge in the Swiss Alps (Beer et al., 2017). They suggested that moving bedload particles are laterally deflected when interacting with these roughness elements, thereby increasing the frequency of impacts on the walls and their erosion rate. However, this interaction has not yet been systematically studied, because previous experiments (e.g., Finnegan et al., 2007; Fuller et al., 2016; Mishra et al., 2018; Shepherd, 1972) and field observations (e.g., Beer et al., 2017; Turowski et al., 2008) focused on reach-scale dynamics, where many processes are concurrently active and feedback on each other.

Within the present paper, we describe experiments designed to isolate the interaction of individual moving bedload particles with roughness elements fixed on the channel bed. We released single bedload particles into a flume channel with a rectangular roughness zone covering half of the channel width, within which hemispherical roughness elements were fixed in a regular square pattern. We recorded individual particle trajectories to systematically investigate how the spacing and size of immobile roughness elements affect sideward deflection of bedload particles and discuss the implications to the lateral erosion of straight bedrock channels with a localized roughness zone.

2. Methods

2.1. Experimental Setup and Protocol

We are interested in the first-order relationship of sideward deflection of bedload particles with the size and spacing of roughness elements. Our approach was to simplify processes and geometric patterns in the experimental design. Therefore, we used single spherical bedload particles that interacted with hemispherical roughness elements, placed in a rectangular pattern in the roughness zone that extends over half of the width of the flume (Figure 1). As a result, our parameters were not scaled to a specific natural river channel.

The flume experiments were conducted at the German Research Center for Geosciences (Potsdam, Germany) in a wooden flume with a slope of 3% (Figure 1). The length and width of the flume were 150 and 40 cm,

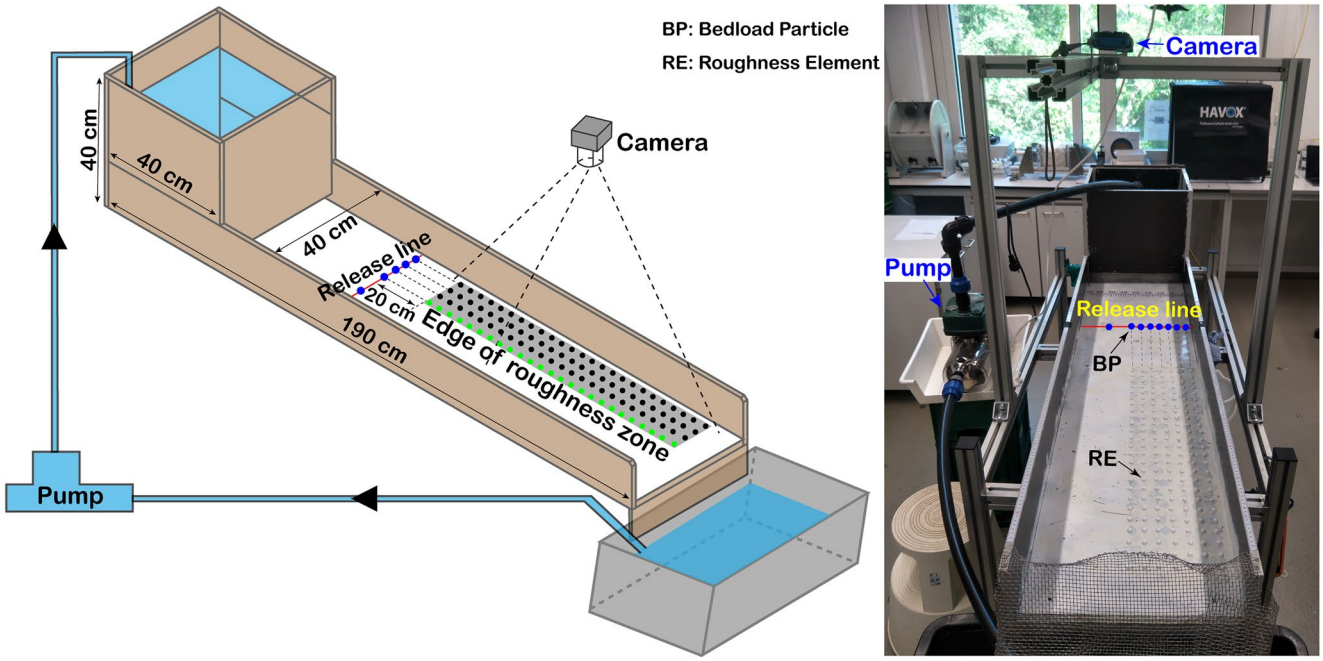

Figure 1. Experimental flume schematic and photo. The flume was made of wooden plates with a thickness of 1.6 cm. The hemispheric roughness elements were stuck on the riverbed with water-proof glue. The length and width of the roughness zone were about 70 and 20 cm, respectively. The pump was a DAB ACTIV El 40/80 M, with a power of 1.48 KW. The diameter of the water pipe was 32 mm. The camera was a Canon PowerShot D30, with a video resolution of 1,920×1,080 pixels. The red line marks the release line located 20 cm upstream of the roughness zone. The edge of the roughness zone was marked by green roughness elements in the schematic illustration.

respectively. Black glass spheres with a diameter of 10 mm were used as bedload particles, while white glass hemispheres with three diameters (5, 10, and 20 mm, Figure S1) were used as roughness elements. The flume bed was painted white to allow easy tracing of the black bedload particles. Bedload particles and roughness elements were produced by a glass bead manufacturer in Germany (Schäfer Glas, https://www.schaeferglas.com), and had a density of 2.54 g/cm^3. For each size of the roughness element, we designed seven rectangular roughness element patterns with an edge-to-edge spacing of 5, 10, 20, 30, 40, 50, and 60 mm. Accordingly, roughness elements were glued onto the riverbed with varying spacing and size in different experiments (Table S1; Figure S2). Water was circulated at a constant discharge of 1.6 L/s for all the 21 sets of experiments, yielding a flow depth of ~1.5 cm in the bare flume. Based on the discharge, the flume width of 40 cm, and the flow depth of 1.5 cm, we estimated the channel-averaged flow velocity at 26.7 cm/s.

The Reynolds number Re ($= \rho uh/\nu = 4{,}005$) quantifies the ratio of turbulent to viscous forces in the flow, where ρ is the fluid density (1 g/cm^3), u is the flow velocity, h is the flow depth, and ν is the viscosity of water (10^{-3} Pa·s). Generally, $Re > 1{,}000$ represents fully turbulent flow (Lamb et al., 2015). The Froude number Fr ($= u/\sqrt{gh} = 0.7$) quantifies the ratio of inertial to gravitational forces, where $g = 9.8$ m/s^2 is the gravitational acceleration (Johnson & Whipple, 2010; Lamb et al., 2015). The threshold value of $Fr = 1$ separates supercritical flow ($Fr > 1$) from subcritical flow ($Fr < 1$) (Lamb et al., 2015). The values of Re and Fr indicate that our flume experiments are in the turbulent and subcritical regimes.

A single bedload particle was released from the release line across the flume, 20 cm upstream of the roughness zone (Figure 1). To ensure the impact of bedload particles with a roughness element at the edge of the roughness zone, release locations were located directly upstream of the columns of roughness elements. As a result, the number of release locations varied for different experiments (Table S1; Figures 2 and S2). From each release location, 10 bedload particles were released (Figure S2). To ensure the presence of a single particle within the flume at each time, a subsequent bedload particle was released after the preceding bedload particle was collected in a steel net fixed to the end of the flume. The movements of bedload particles were recorded continuously with a video camera located above the flume (Figure 1).

2.2. Data Processing

The path of bedload particles was recorded on video by the camera. The area captured by the camera was the same for all the experiments. Pictures were extracted from the video every 0.1 s using a Python script. Pictures have a resolution of 1920×1080, and each pixel corresponds to real size of 0.564 × 0.564 mm at the flume bed. Using a MATLAB script (see Code Availability), the location of bedload particles was marked manually on the pictures and the coordinates were extracted. From the time stamp of the picture and the time series of coordinates, we rebuilt the trajectory, and calculated velocity, deflection distance, and times of impacts.

2.3. Parameters Used to Describe the Motion of Bedload Particles

The lateral erosion rate is controlled by impact velocity, impact rate, the mass and shape of bedload particles, rock strength, weathering intensity, and fluid shear stress (Lamb et al., 2008, 2015; Li et al., 2020, 2021; Sklar & Dietrich, 2004; Small et al., 2015; Turowski, 2020). The focus of our experiments is the interaction of moving bedload particles with roughness elements. After the impacts with roughness elements, particles slow down on the way to the banks due to the resistance from the water and flume bed. Thus, if the particle moves unobstructed after interacting with a roughness element, the impact velocity relevant for lateral bedrock erosion is determined by this interaction and the distance from the wall. To introduce measurable parameters effectively, we name the direction along and perpendicular to the flume the X and Y direction, respectively. We measured the number of Y-direction changes (a proxy of impact times), the maximum travel distance in the Y-direction, the total distance traveled in the Y-direction, the total traveled distance, as well as the maximal and average Y-direction velocity to learn about the deflection length and velocity. Each of these parameters can easily be measured in our experiments and is explained in more detail in the Supporting Information S1.

3. Results

3.1. Trajectories of Bedload Particles

Particles predominantly tended to roll in our experiments, with occasional small saltations. The trajectories of bedload particles for all experiments are displayed in Figure 2. For the smallest roughness element spacing of 5 mm, bedload particles were likely to be stopped by roughness elements, with stopping locations moving upstream as roughness element size increased. Specifically, for a roughness element size of 5 mm, more than half of the bedload particles moved through the entire length of the roughness zone (Figure 2a). For a roughness element size of 10 mm, bedload particles reached the end of the flume if they laterally left the roughness zone after the first impact with a roughness element. Bedload particles that remained in the roughness zone eventually stopped (Figure 2a). For a roughness element size of 20 mm, 35 out of 40 bedload particles stopped upon the first impact with a roughness element, while the remainder laterally left the roughness zone after the first impact (Figure 2a). For a roughness element spacing greater than 5 mm, all bedload particles moved through the roughness zone and eventually left the flume. After the first impact with a roughness element, the downstream velocity of bedload particles decreased rapidly (Figure 3). Bedload particles were deflected laterally, with an equal probability to be deflected to the left or right. As long as bedload particles were in the roughness zone, they repeatedly collided with roughness elements, changing their velocities upon impacts. By contrast, a fraction of bedload particles laterally left the roughness zone after one or more impacts. The trajectories of these bedload particles follow a smooth curve after leaving the roughness zone, with decreasing cross-channel velocity and increasing downstream velocity. About half of the bedload particles that were released directly above the edge of the roughness zone laterally left the roughness zone after the first impact with a roughness element. The remaining half moved to the left into the roughness zone but showed an average probability of 17.1% of laterally leaving the roughness zone after later impacts. The degree of concentration of trajectories is largely influenced by the spacing and size of roughness elements. Trajectories tended to concentrate on small roughness element spacing and large roughness element size.

Figure 2. The trajectories and velocities of bedload particles for the 21 sets of experiments. The trajectories of 10 bedload particles were shown in the figure for all the release locations, including the one above the edge of the roughness zone. Locations were mapped every 0.1 s. See Figure S2 for a detailed setup of the roughness zone and the release locations for the 21 sets of experiments. The upper and lower boundary of the figure is channel walls.

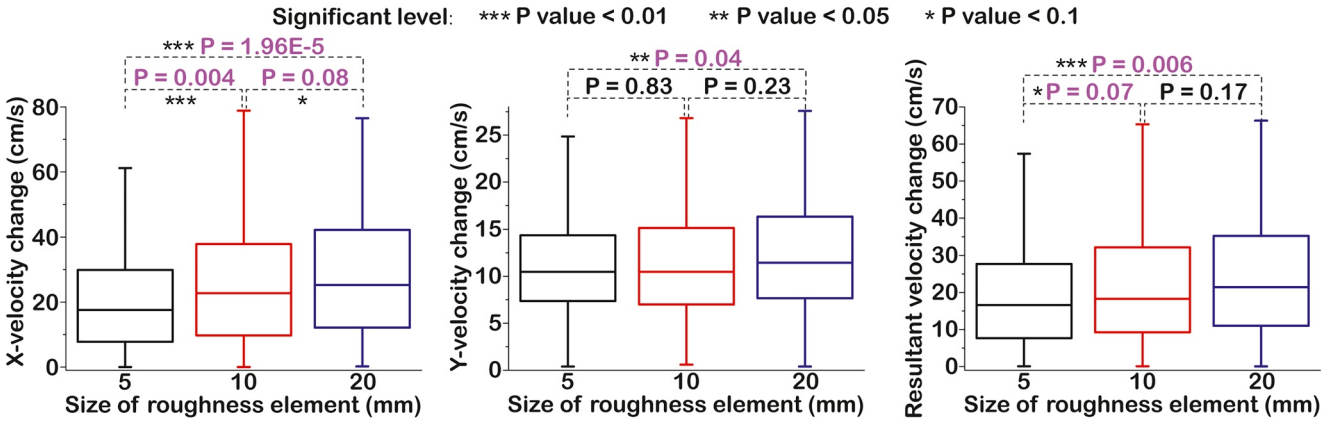

Figure 3. Boxplots show the velocity change of bedload particles after the first impact with roughness elements. Kolmogorov–Smirnov tests demonstrate that, in many cases, the size of the roughness element has a significant influence on the velocity change after the first impact.

3.2. Sideward Deflection

When bedload particles interacted with roughness elements, their cross-channel direction of motion and velocity changed (Figures 2–4). Velocity changes caused by the first impact increase with the size of roughness elements (Figure 3). Except for three experiments (roughness element spacing of 5 mm, roughness element sizes of 5, 10, and 20 mm) during which most bedload particles stopped within the roughness zone, the normalized *Y*-direction change times decreased with increasing roughness element spacing (Figure 4a). For roughness element size of 10 mm, the maximal *Y*-direction distance peaks at roughness element spacing of 50 mm and then decreases from spacing 50–60 mm. Meanwhile, for roughness element sizes of 20 mm, the maximal *Y*-direction distances increased with the increasing spacing of roughness elements (Figure 4b). The total *Y*-direction distances increased with increasing roughness element spacing

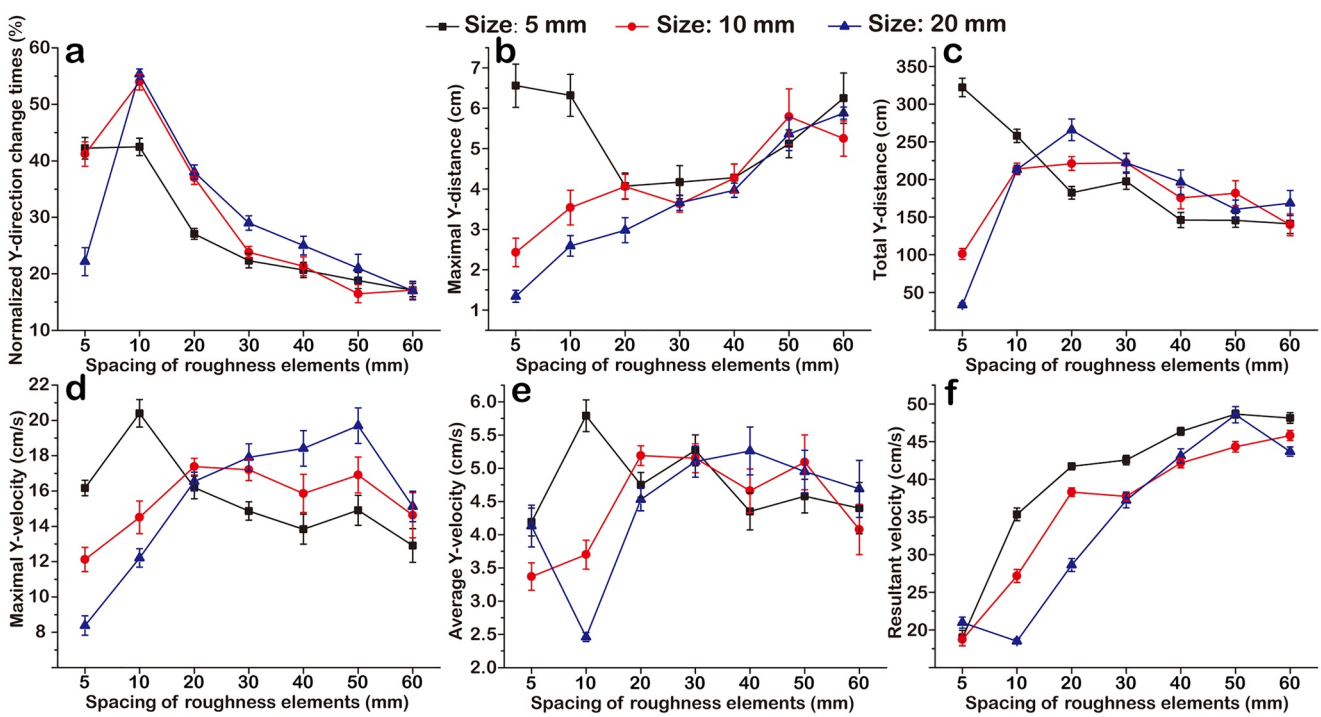

Figure 4. Statistics of particle motion as a function of spacing and size of roughness elements. (a) Normalized *Y*-direction change times, (b) maximal *Y*-distance, (c) total *Y*-distance, (d) maximal *Y*-velocity, (e) average *Y*-velocity, and (f) resultant velocity varies with the spacing of roughness elements. Errors are the standard error of the mean. See methods for the definitions of the parameters.

and reached the highest values at a spacing of 20 mm before it decreased again (Figure 4c). For a roughness element size of 5 mm, when roughness element spacing was 5 and 10 mm, bedload particles frequently jumped over roughness elements leading to large maximal *Y*-direction distance and total *Y*-direction distance (Figures 4b and 4c). The maximal *Y*-direction distance decreased with increasing spacing until spacing reached 30 mm, then it increased with increasing spacing. Meanwhile, with the increase of roughness element spacing, the probability of impact decreased rapidly (Figure 4a), decreasing the total *Y*-direction distance (Figure 4c).

The experiments with the three different roughness element sizes show similar patterns in the maximal *Y*-velocity, that is, an increase to peak values, then a decrease with increasing roughness element spacing (Figure 4d). Peak values were reached at a roughness element spacing of 10 mm for a size of 5 mm, at a spacing of 20 mm for a size of 10 mm, and at a spacing of 50 mm for a size of 20 mm. Overall, the average *Y*-velocity shows a similar pattern as the maximal *Y*-velocity (Figure 4e). Resultant velocity increased with increasing roughness element spacing (Figure 4f).

3.3. Escape From the Roughness Zone

Bedload particles released directly above the edge of the roughness zone showed the highest probability (≥50%) of laterally escaping from the roughness zone (Figures 5a and 5b). The probability decreased with the increase of *Y*-direction distance between the edge of the roughness zone and release location. When the distance reached 9 cm, only 1 out of 430 bedload particles was able to leave the roughness zone. The Kolmogorov-Smirnov test shows that these observed differences are significant at the 1% level. There is a lot of scattering for the different experimental configurations (Figure 5a), but a clear trend emerges when all data are averaged (Figure 5b). If we assume that particle motion is analogous to Brownian motion with diffusivity D in the transverse direction when inside the roughness zone, according to Balakrishnan (2021), the probability density that a particle that started a distance x from the edge of the roughness zone exits after a time t is

$$f\left(t,x\right)=\frac{x}{\sqrt{4\pi Dt^{3}}}\exp\left(-\frac{x^{2}}{4Dt}\right). \tag{1}$$

The cumulative exit probability given the particle started a distance x from the edge of the roughness zone for any available travel time T is then

$$y=\int_{0}^{T}f\left(t,x\right)dt=erfc\left(\frac{x}{\sqrt{4DT}}\right). \tag{2}$$

Therefore, we can fit the exit probability data with a complementary error function $y = Aerfc(Bx)$ in analogy to the exit probabilities of diffusing particles. We obtain values of $A = 58.18$ and $B = 0.17$, with $R^2 = 0.85$ (Figure 5a). In general, the probability of leaving the roughness zone increases with the spacing of roughness elements (Figure 5c). For small roughness elements with a diameter of 5 mm, there is a significantly higher probability of leaving the roughness zone compared with larger roughness elements (Figure 5d).

A total of 158 bedload particles left the roughness zone after one or more impacts with roughness elements. Figure 6 demonstrated the *Y*-velocity characteristics of these particles. Within the roughness zone, the *Y*-velocity of these particles changed randomly. In contrast, it declined systematically after leaving the roughness zone (Figures 6a–6i). Particles released above the edge of the roughness zone had a *Y*-velocity of 15.2 ± 0.6 cm/s when leaving the roughness zone (Figure 6j). At the time of leaving the roughness zone, the *Y*-velocity increased to its peak value of 17.2 ± 1.6 cm/s for the particles released near the edge of the roughness zone. Then, *Y*-velocity decreased with the *Y*-distance between the release location and the edge of the roughness zone.

4. Discussion

4.1. Controls on the Sideward Deflection of Bedload Particles

Except for the case of roughness elements of the size of 20 mm, in which the maximum *Y*-distance increased with spacing, we observed non-monotonic relationships between the *Y*-direction change times (Figure 4a),

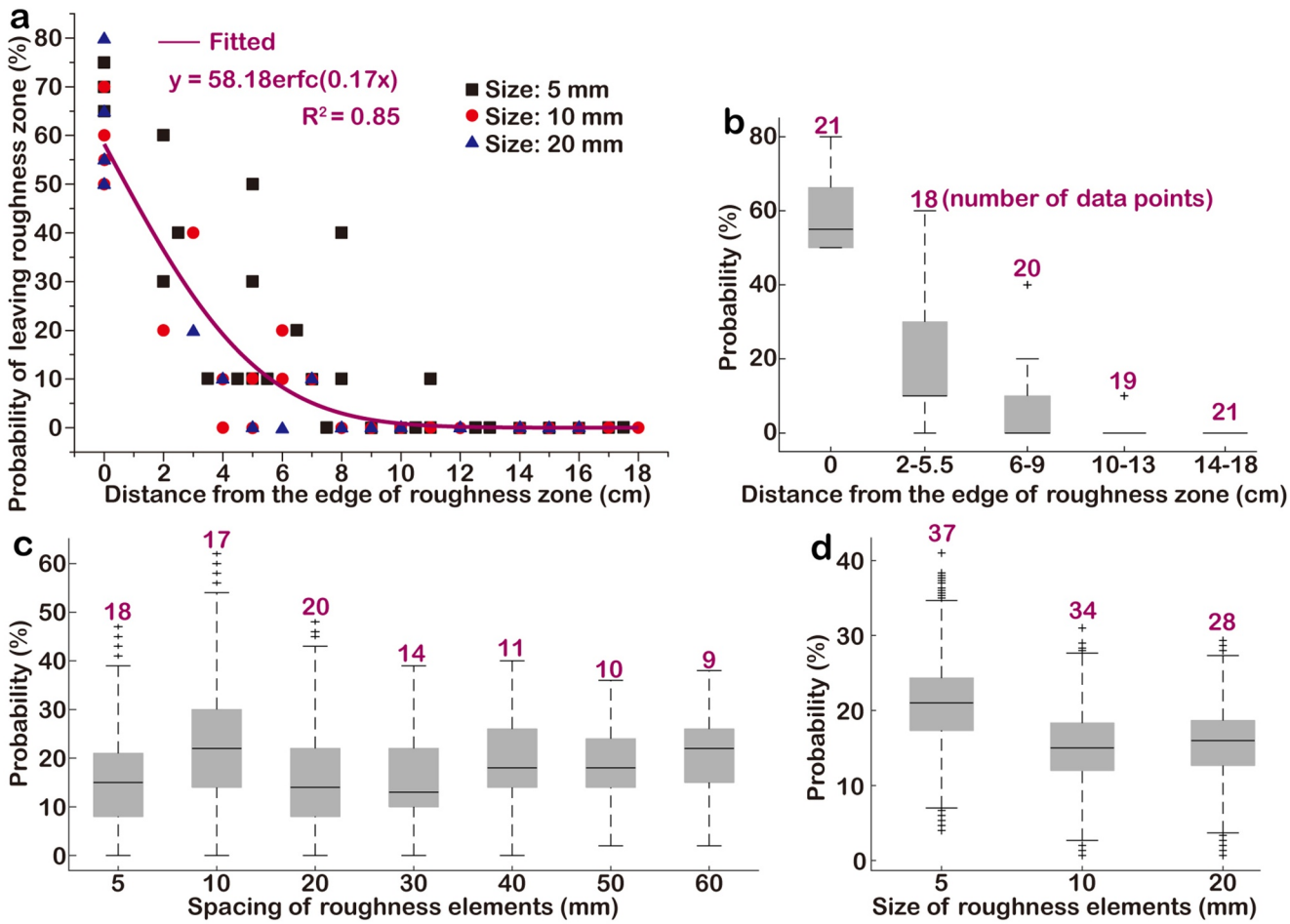

Figure 5. The probability of bedload particles leaving the roughness zone. (a) The probability of leaving the roughness zone decreases with the distance from the edge of the roughness zone for each experimental configuration. (b) Boxplots summarize data. (c) Boxplots show the probability of leaving the roughness zone in the different spacing of roughness elements. We randomly sampled five values of the seven datasets individually and calculated the average of five values. This was repeated 10,000 times to construct the plots. (d) Boxplots show the probability of leaving the roughness zone in different sizes of roughness elements. We randomly sampled 15 values of the three datasets individually and calculated the average of the 15 values. This was repeated 10,000 times to construct the plots.

the maximal and total motion in the cross-channel direction (Figures 4b and 4c), and the maximum and average cross-channel velocity (Figures 4d and 4e) with roughness element spacing. The observed humped function arises out of the competition between the length of the free path, which increases with increasing roughness element spacing, and the probability of a bedload particle to impact a roughness element per unit length, which decreases with increasing roughness element spacing. As such, roughness element spacing has a dual role. Roughness elements make sideward motion possible in the first place, but also inhibit further lateral motion due to the limited free path. For large roughness spacing, the path is free for lateral movement, but low impact probability per unit length limits the chance for sideward deflection in the first place. As an example, in our experiments, for roughness element sizes of 10 and 20 mm, the probability of impact is high for small roughness element spacing (Figure 4a). However, the sideward deflection of bedload particles is limited by the small distance available for lateral motion. As a result, the overall sideward deflection distance is small (Figures 4b and 4c). With the increase of spacing, the total *Y*-direction distance increased (Figure 4c), despite the decrease of the impact probability (Figure 4a). Then, even though the spacing increased further, the total *Y*-direction distance decreased (Figure 4c) as does the decrease of impact probability (Figure 4a).

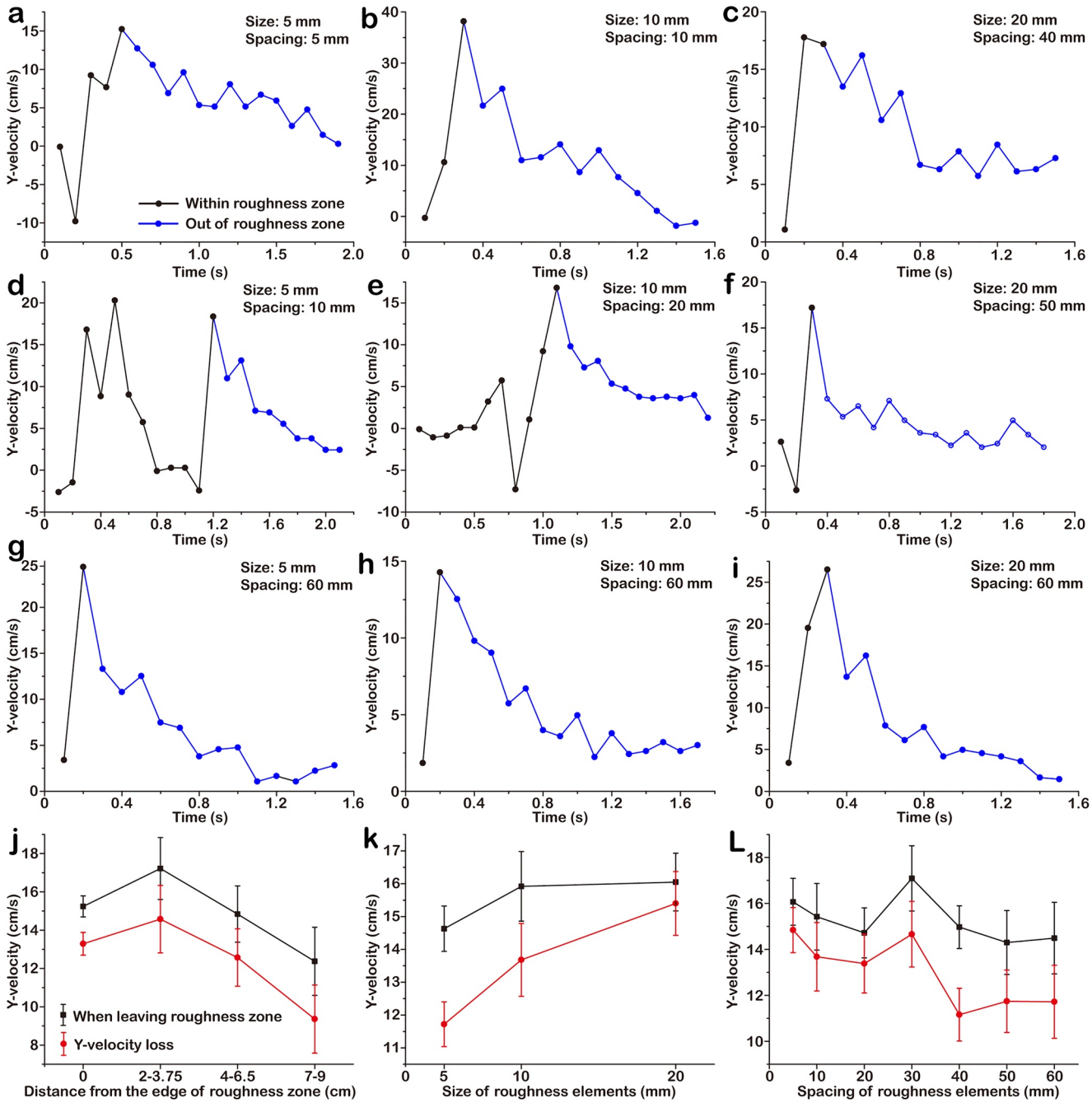

Figure 6. (a)–(i) The *Y*-velocities of the representative bedload particles that leave the roughness zone. Positive *Y*-velocity means moving toward the right channel wall (looking downstream). (j)–(l) The *Y*-velocity when leaving the roughness zone and *Y*-velocity loss between leaving the roughness zone and leaving the flume.

A similar dual role of the influence of roughness on particle sideward deflection has been suggested by Turowski (2018, 2020), who argued that sideward deflection is most efficient at the edge of alluvial deposits into the direction of the bare bedrock. There, roughness elements facilitate sideward deflection of moving particles, but because bare bedrock is smooth, sideward motion is not hindered and lateral motion distances and velocities are maximized. The existence of an optimal roughness element spacing and size to achieve maximal lateral erosion rate agrees with predictions by Li et al. (2020), who modeled the deflection of individual particles by roughness elements and their effect on lateral erosion. Flume experiments also

demonstrate a roughly parabolic relation between the roughness element size/space and lateral erosion rate (Fuller et al., 2016). We expect that this optimal spacing is a function of the hydraulics, morphology, and sediment characteristics of a particular river. Further research is necessary to fully unravel these controls.

In our experiments, for the smallest roughness element size of 5 mm and a roughness element spacing of 5 and 10 mm, bedload particles frequently jumped over roughness elements to achieve maximal *Y*-direction distances (Figures 4b and 4c) and a relatively high probability of leaving the roughness zone (Figure 5d). The occurrence of this behavior thus seems to depend on the relative size of bedload particles and roughness elements, but also on the relative flow depth, which limits the space bedload particles have available for motion in the vertical direction. The relatively low flow depth of ~1.5 cm in our experiments, implying that the size of bedload particles and roughness elements is similar to flow depth, which inhibits the saltation of bedload particles. For deep rivers, especially those with high flow velocity and thus high transport stage, a large fraction of bedload particles may be saltating downstream (Auel et al., 2017). This is likely especially important for steep mountain rivers during floods. However, how the possibility of saltation affects the sideward deflection of bedload particles in deep bedrock rivers requires further research. Flow velocity and channel slope also impact the likelihood of saltation and particle trajectories, with saltation becoming more frequent as flow velocity or slope increase (Auel et al., 2017). The low flume-averaged flow velocity of 26.7 cm/s and a fixed flow depth and flume slope prevent us from systematically investigating these controls and further experiments will be necessary.

The *Y*-velocity when leaving the roughness zone is crucial for wall erosion. When leaving the roughness zone, it is determined by the inherited *Y*-velocity and the *Y*-velocity gain from the last impact with roughness elements at the edge of the roughness zone. It can be expected that the larger the distance between the release location and the edge of the roughness zone is, the lower will be the resultant velocity and inherited *Y*-velocity when reaching the edge of the roughness zone. This is because particles need more impacts to reach the edge of the roughness zone, and each impact will reduce the resultant velocity. For particles released above the edge of the roughness zone, most of the *Y*-velocity when leaving the roughness zone came from the last impact with roughness elements, because their inherited *Y*-velocity is negligible. However, for particles released 2–4 cm from the edge of the roughness zone, they have the largest inherited *Y*-velocity and high *Y*-velocity gain from the last impact, thus, they have the highest *Y*-velocity when leaving the roughness zone (Figure 6j). For particles released far away (>4 cm) from the edge of the roughness zone, the inherited *Y*-velocity and *Y*-velocity gain from the last impact are low, because the resultant velocity is low due to frequent impacts before reaching the edge of the roughness zone.

Y-velocity when leaving the roughness zone increased from 14.6 ± 0.7 cm/s for roughness elements size of 5 mm to 16.1 ± 0.9 cm/s for roughness elements size of 20 mm (Figure 6k). The reason that *Y*-velocity when leaving the roughness zone increased with the size of roughness elements is that the smaller the roughness elements, the more likely the particles can jump over the roughness elements, and thus lower *Y*-velocity gain. When the roughness element spacing is 30 mm, the *Y*-velocity when leaving the roughness zone reached the peak value of 17.1 ± 1.4 cm/s. For all the 158 particles that left the roughness zone, 114 particles were released above the edge of the roughness zone. For these 114 particles, the *Y*-velocity gain from the last impact was not influenced by the spacing of roughness elements, and this is the reason why there is a lack of systematic relationship between roughness element spacing and *Y*-velocity when leaving the roughness zone (Figure 6l). *Y*-velocity loss has a similar trend as the *Y*-velocity when leaving the roughness zone (Figures 6j–6l). The relatively low video frame rate (10 Hz) is expected to induce additional uncertainty contributed by localization error, which we consider not a major issue, as the focus of this work is exploring first-order characteristics of bedload sideward deflection.

4.2. Upscaling to Natural Rivers

In a natural stream, roughness elements are unlikely to be regularly spaced, or have uniform sizes, as in our experiments and in the model of Li et al. (2020). Roughness element size and spacing are determined by the feedback between bedrock erosion, hydraulics, and sediment transport, and are likely strongly determined by lithological properties (e.g., Richardson & Carling, 2005). This feedback, the physical details of the formation of bedrock bedforms, and their lithological controls are still poorly understood (e.g., Richardson &

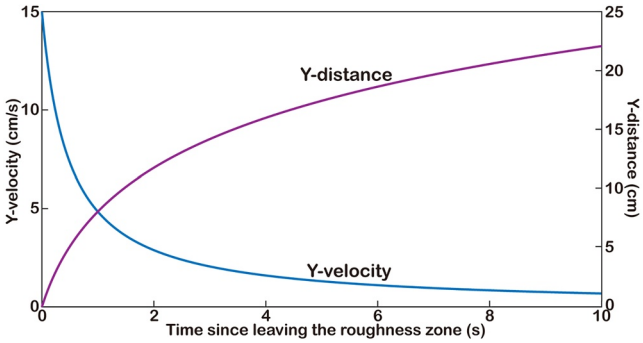

Figure 7. The *Y*-distance and *Y*-velocity varied with time since bedload particles leaving the roughness zone, based on the drag equation.

Carling, 2005; Wilson et al., 2013). Alluvial deposits self-organize in response to local conditions, including flow velocity, turbulence, and channel morphology (e.g., Dreano et al., 2010; Hodge et al., 2016; Johnson & Whipple, 2010; Mishra et al., 2018). Similar to the simulation experiments by Li et al. (2020), we used spherical bedload particles and hemispherical roughness elements in our flume experiments. Given that the simulation experiments by Li et al. (2020) have well reproduced the lateral erosion patterns observed in flume experiments by Fuller et al. (2016), which used nonspherical roughness elements, the influence of nonspherical natural particles on lateral erosion patterns may be negligible (e.g., Li et al., 2020), although they can be expected to affect erosion rates. Scale effects arise due to force ratios that are not identical between a model and its real-world prototype and result in deviations between the model and prototype observations (Heller, 2011). Scaling behavior and the evolution of *Y*-distance and *Y*-velocity after leaving the roughness zone can be estimated by a simple force balance between inertia and drag. The drag force (F) can be described by the drag equation as

$$F = -\frac{1}{2}\rho_w ACV^2, \tag{3}$$

where ρ_w is water density (1 g/cm^3), A is the cross-sectional area of the particle (0.79 cm^2), C is a drag coefficient with a value of 0.47 for spheres in water, and V is the *Y*-velocity. The acceleration (a) of the particle is

$$a = \frac{dV}{dt} = \frac{F}{m} = -\frac{\rho_w ACV^2}{2m}, \tag{4}$$

where m is the mass of bedload particle (1.32 g). Then we have

$$\int_{V_0}^{V} \frac{1}{V^2} dV = \int_0^t -\frac{\rho AC}{2m} dt, \tag{5}$$

where V_0 is the initial *Y*-velocity when leaving the roughness zone. Accordingly, the *Y*-velocity is given by

$$V = \frac{V_0}{1 + \frac{\rho_w ACV_0}{2m} t} = \frac{V_0}{1 + \frac{3}{4}\frac{\rho_w CV_0}{\rho_b d} t}. \tag{6}$$

In Equation 6, ρ_b is the density of bedload particle (2.54 g/cm^3), and the right-hand equality gives the equation for a sphere with diameter d. Integrating a second time, the *Y*-distance (S) can be described as

$$S = \int_0^t \frac{V_0}{1 + \frac{\rho_w ACV_0}{2m} t} dt = \frac{2m}{\rho_w AC} \ln\left(\frac{\rho_w ACV_0}{2m} t + 1\right) = \frac{4}{3}\frac{\rho_b d}{\rho_w C} \ln\left(\frac{3}{4}\frac{\rho_w CV_0}{\rho_b d} t + 1\right). \tag{7}$$

When written in terms of particle diameter, the particle trajectory depends only on the initial velocity, the particle diameter, the drag coefficient, and the density ratio of water and bedload (Equations 6 and 7). The drag coefficient can be considered to be constant for fully turbulent flow with a Reynolds number $Re > 1{,}000$ (e.g., Timmerman & van der Weele, 1999), which is the case both for our experiments and most natural rivers. The deflection velocity, V_0, likely depends on particle speed before impact, which is determined by hydraulics, and roughness size and shape. Some scaling can be expected for this parameter, however, the densities of the fluid and the particles, as well as the particle velocities in our experiments are similar to those observed in natural flows.

Based on Equations 6 and 7, the *Y*-velocity decreases over time (Figure 7), comparable with our results (Figures 6a–6i). In our experiments, the average V_0 when leaving the roughness zone for the 158 particles that left the roughness zone was 15 cm/s. Thus, the *Y*-distance is predicted to be 22 cm at 10 s (Figure 7), similar to the value measured in our experiments (Figure 2). The observed (Figure 2) and predicted (Figure 7) trajectories indicate that a larger distance between the edge of the roughness zone and the channel wall causes wall erosion to be located further downstream from the point of deflection, as more time is needed to reach and impact the wall, a phenomenon also shown by Li et al. (2020).

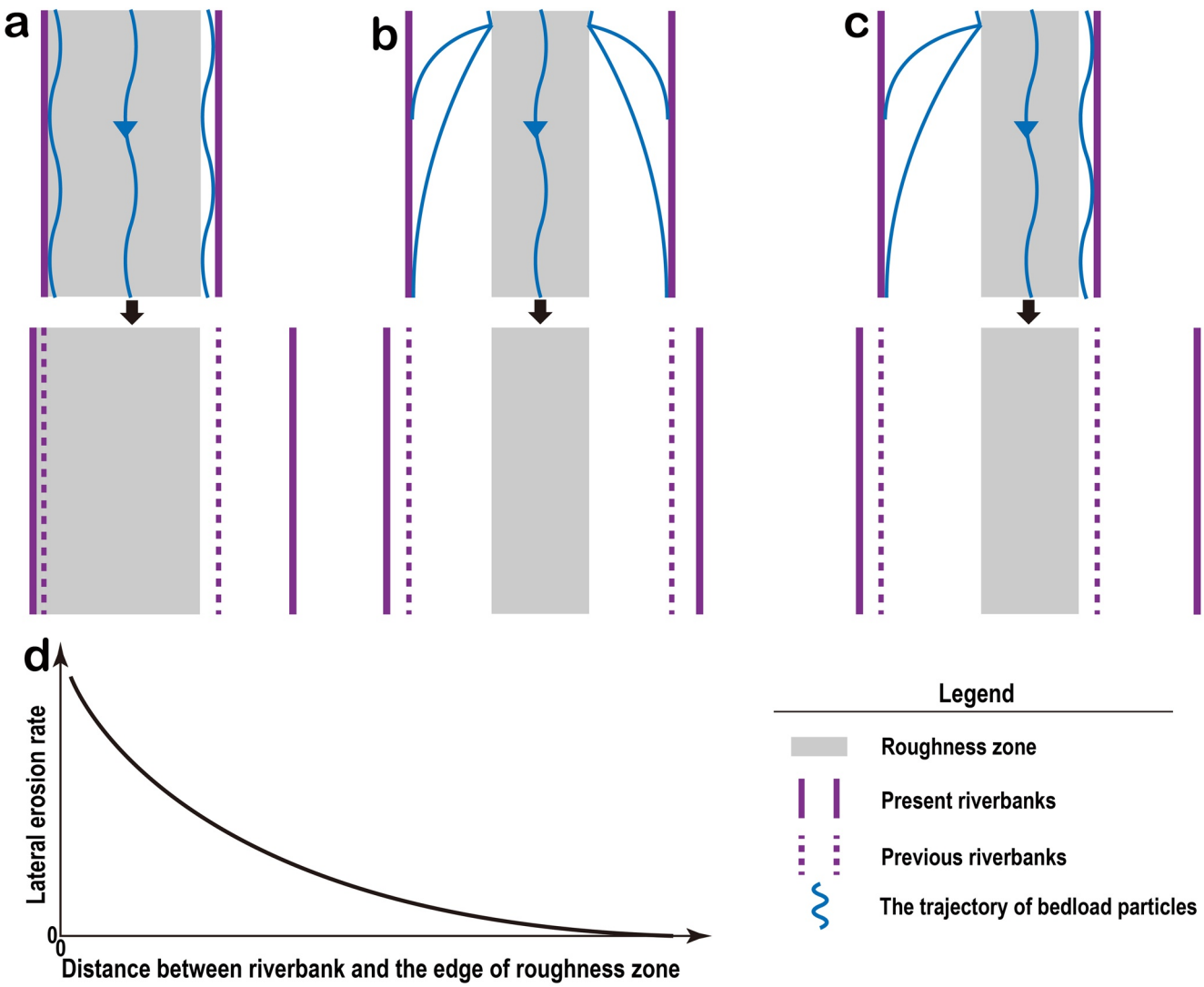

Figure 8. Illustration of how bedrock channels are laterally eroded in different settings of roughness zone under the condition that bedload particles cannot jump over roughness elements. The white area within the riverbed is a bare bedrock riverbed, and the gray area depicts stationary alluvial cover. (a) The riverbed is fully covered by alluvial deposits, except a small area of the bare riverbed. (b) The roughness zone is located at the center of the riverbed. (c) The roughness zone is located closer to one of the riverbanks than to the other. (d) Schematic relationship between lateral erosion rate and the distance between the riverbank and the edge of the roughness zone.

4.3. Implications for Lateral Erosion

For straight partially alluviated bedrock channels, there are two options for the deflected bedload particles to cause bedrock wall erosion. First, they may move on the alluvial deposit close to a bedrock wall (Figure 8a). Second, they may escape from the roughness zone to travel laterally over smooth bedrock (Figures 8a–8c) (cf. Turowski, 2018, 2020). In natural rivers, bedload transport is not uniform across the channel but is concentrated along a sinusoidal path in the downstream direction (Bunte et al., 2006; Dietrich & Smith, 1984; Julien & Anthony, 2002). As a consequence, sideward deflection and lateral erosion can be expected to be effective at the locations where the bedload path interacts with stationary alluvial patches, in particular where it crosses from an alluvial patch onto the bare bedrock bed (cf. Turowski, 2018). Our flume experiments show that the probability of leaving the roughness zone decreases with the distance between the edge of the roughness zone and the release location (Figure 5). After being deflected by a roughness element, bedload particles need to travel laterally to impact the riverbank. The cross-channel velocity decreases due to drag (Figures 2 and 7). The larger the distance is between the riverbank and the edge of the roughness

zone, the less remnant cross-channel energy is available to cause lateral erosion, as demonstrated by recent numerical simulations (Li et al., 2020) (see also Equation 6). Particularly, if the distance between the edge of the roughness zone and the channel wall exceeds a certain value, wall erosion may never happen, because bedload particles cannot reach the walls. As a result, the increase of the distance between the edge of the roughness zone and the wall not only decreases the number of particles impacting the wall but also reduces the lateral momentum of particles (Figures 7 and 8).

On the condition that bedload particles are unable to jump over roughness elements and there is a bare riverbed between the riverbank and the edge of the roughness zone for bedload particles to move, we expect a negative correlation between lateral erosion rate and the distance between the riverbank and the edge of the roughness zone (Figure 8d), a similar result has been observed in simulation experiments (Li et al., 2020). Accordingly, we can distinguish three major cases in a simplified concept for the interplay between alluvial cover and bedrock river lateral erosion. First, a riverbed is fully covered by alluvial deposits, except for a small area of bare riverbed (Figure 8a). Bedload particles near the riverbank on the uncovered side can impact the wall frequently, and the majority of their kinetic energy can be expended in lateral bedrock erosion. In contrast, bedload particles near the riverbank on the covered side can hardly impact the wall, because the roughness elements that contact the wall can protect the wall from impacts, and diffusive motion over the alluvium leads to small lateral particle velocities (cf. Seizilles et al., 2014). In this case, the two banks experience different erosion rates. Second, when the roughness zone is located at the center of the riverbed, both riverbanks are eroded at a similar rate (Figure 8b). Third, when the roughness zone is located closer to one of the riverbanks, this bank will experience a higher erosion rate, provided that the bedload concentration is symmetric across the channel. In this case, due to the erosion rate difference between the two riverbanks, the channel evolves such that the roughness zone is located at its center (Figure 8c). The erosional adjustment of channel morphology, in turn, changes flow patterns, and therefore the location of the bedload path and alluvial deposits (e.g., Finnegan et al., 2007; Mishra et al., 2018). The formation of alluvial bedforms and the bedload path on partially covered beds are incompletely understood and need further research (e.g., Dreano et al., 2010; Hodge et al., 2016; Jafarinik et al., 2019; Johnson & Whipple, 2010; Mishra et al., 2018). Therefore, the simplified first-order model of channel widening in response to the size and location of the roughness zone suggested here (Figure 8) needs to be validated with laboratory experiments and field observations.

5. Conclusions

The sideward deflection distance and velocity of bedload particles were explored by 21 sets of flume experiments with different spacings and sizes of roughness elements. Velocity changes caused by the first impact increase with the size of roughness elements. The length of the free path available for bedload particles to move and the impact probability between bedload particle and roughness element are two main factors that determine the sideward motion of bedload particles. Both of these two factors are necessary for bedload particles to achieve a high deflection length and velocity. The length of the free path increases with increasing roughness element spacing, while the impact probability decreases with increasing roughness element spacing. The optimal spacing to gain the maximal sideward deflection length and velocity can be expected to be a function of hydraulics, morphology, and the sediment characteristics of a particular river. Further research is necessary to unravel these controls. The size of roughness elements affects the sideward deflection of bedload particles in two ways. First, in combination with the size of the roughness elements, the roughness element spacing determines the length of the free path. Second, the relative size of bedload particles and roughness elements determines whether bedload particles can jump over or are stopped by roughness elements. The relative flow depth and flow velocity can also be expected to affect this behavior, which deserves further experiments. The Y-velocity declined after leaving the roughness zone. Y-velocity when leaving the roughness zone reached the peak value for the particles released near the edge of the roughness zone, and it increased with the size of roughness elements.

In straight partially alluviated bedrock channels, there are two ways for deflected bedload particles to cause lateral erosion. First, they may move on the alluvial deposit close to a bedrock wall. Second, they may escape from the roughness zone to travel laterally over smooth bedrock. Given our observations on a sideward deflection in a straight channel with a localized roughness zone, the lateral erosion rate should show a

negative relationship with the distance between the riverbank and the edge of the roughness zone. As a result, the evolution of such bedrock rivers and their widening rates largely depend on the location and size of roughness zones. However, the formation of alluvial deposits on bedrock beds, the evolution of roughness zones in response to hydraulics, and the bedload path within such a channel need further investigation.

Data Availability Statement

The raw data underlying Figures 2–6 was deposited in Figshare at https://doi.org/10.6084/m9.figshare.12623654.v5. A MATLAB script (Tracking_particles.m) and its related toolbox, a readme file, and a video tutorial that can obtain the time series of coordinates from pictures were deposited at https://doi.org/10.6084/m9.figshare.12623654.v5.

Acknowledgments
The authors are grateful to Markus Reich for flume design and help with its construction, Gunnar Pruß for purchasing roughness elements and bedload particles, as well as building the Python script to extract pictures from videos, Anne Voigtländer for help with installing the pump, and Herve Capart for providing the toolbox used by our MATLAB script (see Code Availability). Thanks go also to Brian J. Yanites and Zhenyu Peng for fruitful discussion, and to the Associate Editor and three anonymous reviewers for comments on previous versions of this paper. C.J. Yang was supported by grants from the Ministry of Science and Technology (Taiwan) (MOST 110-2917-I-564-009). Open access funding enabled and organized by Projekt DEAL.

References

Auel, C., Albayrak, I., Sumi, T., & Boes, R. M. (2017). Sediment transport in high-speed flows over a fixed bed: 1. Particle dynamics. *Earth Surface Processes and Landforms*, *42*, 1365–1383. https://doi.org/10.1002/esp.4128

Balakrishnan, V. (2021). *Elements of nonequilibrium statistical mechanics*. https://doi.org/10.1007/978-3-030-62233-6

Beer, A. R., Turowski, J. M., & Kirchner, J. W. (2017). Spatial patterns of erosion in a bedrock gorge. *Journal of Geophysical Research: Earth Surface*, *122*, 191–214. https://doi.org/10.1002/2016jf003850

Bunte, K., Potyondy, J. P., Abt, S. R., & Swingle, K. W. (2006). Path of gravel movement in a coarse stream channel. Paper presented at the *Proceedings of the Eighth Federal Interagency Sedimentation Conference* (pp. 162–170).

Burbank, D. W., Leland, J., Fielding, E., Anderson, R. S., Brozovic, N., Reid, M. R., & Duncan, C. (1996). Bedrock incision, rock uplift and threshold hillslopes in the northwestern Himalayas. *Nature*, *379*, 505–510. https://doi.org/10.1038/379505a0

Chatanantavet, P., & Parker, G. (2009). Physically based modeling of bedrock incision by abrasion, plucking, and macroabrasion. *Journal of Geophysical Research: Earth Surface*, *114*, F04018. https://doi.org/10.1029/2008JF001044

Cook, K. L., Turowski, J. M., & Hovius, N. (2014). River gorge eradication by downstream sweep erosion. *Nature Geoscience*, *7*, 682–686. https://doi.org/10.1038/ngeo2224

Cook, K. L., Turowski, J. M., & Hovius, N. (2020). Width control on event-scale deposition and evacuation of sediment in bedrock-confined channels. *Earth Surface Processes and Landforms*, *45*, 3702–3713. https://doi.org/10.1002/esp.4993

Dietrich, W. E., & Smith, J. D. (1984). Bed load transport in a river meander. *Water Resources Research*, *20*, 1355–1380. https://doi.org/10.1029/wr020i010p01355

Dreano, J., Valance, A., Lague, D., & Cassar, C. (2010). Experimental study on transient and steady-state dynamics of bedforms in supply limited configuration. *Earth Surface Processes and Landforms*, *35*, 1730–1743. https://doi.org/10.1002/esp.2085

Duvall, A., Kirby, E., & Burbank, D. (2004). Tectonic and lithologic controls on bedrock channel profiles and processes in coastal California. *Journal of Geophysical Research*, *109*, F03002. https://doi.org/10.1029/2003jf000086

Fathel, S. L., Furbish, D. J., & Schmeeckle, M. W. (2015). Experimental evidence of statistical ensemble behavior in bed load sediment transport. *Journal of Geophysical Research: Earth Surface*, *120*, 2298–2317. https://doi.org/10.1002/2015jf003552

Finnegan, N. J., Schumer, R., & Finnegan, S. (2014). A signature of transience in bedrock river incision rates over timescales of 10^4–10^7 years. *Nature*, *505*, 391–394. https://doi.org/10.1038/nature12913

Finnegan, N. J., Sklar, L. S., & Fuller, K. (2007). Interplay of sediment supply, river incision, and channel morphology revealed by the transient evolution of an experimental bedrock channel. *Journal of Geophysical Research*, *112*, F03S11.

Fuller, T. K., Gran, K. B., Sklar, L. S., & Paola, C. (2016). Lateral erosion in an experimental bedrock channel: The influence of bed roughness on erosion by bed load impacts. *Journal of Geophysical Research: Earth Surface*, *121*, 1084–1105. https://doi.org/10.1002/2015jf003728

Gilbert, G. K. (1877). *Geology of the Henry mountains (Utah)*: USGS Report, Government Printing Office.

Hartshorn, K., Hovius, N., Dade, W. B., & Slingerland, R. L. (2002). Climate-driven bedrock incision in an active mountain belt. *Science*, *297*, 2036–2038. https://doi.org/10.1126/science.1075078

He, C. Q., Rao, G., Yang, R., Hu, J. M., Yao, Q., & Yang, C.-J. (2019). Divide migration in response to asymmetric uplift: Insights from the Wula Shan horst, North China. *Geomorphology*, *339*, 44–57. https://doi.org/10.1016/j.geomorph.2019.04.024

He, C. Q., Yang, C.-J., Turowski, J. M., Rao, G., Roda-Boluda, D. C., & Yuan, X. P. (2021). Constraining tectonic uplift and advection from the main drainage divide of a mountain belt. *Nature Communications*, *12*, 544. https://doi.org/10.1038/s41467-020-20748-2

Heller, V. (2011). Scale effects in physical hydraulic engineering models. *Journal of Hydraulic Research*, *49*, 293–306. https://doi.org/10.1080/00221686.2011.578914

Hodge, R., Hoey, T. B., Maniatis, G., & Lepretre, E. (2016). Formation and erosion of sediment cover in an experimental bedrock-alluvial channel. *Earth Surface Processes and Landforms*, *41*, 1409–1420. https://doi.org/10.1002/esp.3924

Inoue, T., Mishra, J., & Parker, G. (2021). Numerical simulations of meanders migrating laterally as they incise into bedrock. *Journal of Geophysical Research: Earth Surface*, *126*, e2020JF005645. https://doi.org/10.1029/2020JF005645

Jafarinik, S., Moreira, R. H., & Viparelli, E. (2019). Alluvial morphodynamics of bedrock reaches transporting mixed-size sand. Laboratory experiments. *Journal of Geophysical Research: Earth Surface*, *124*, 3067–3089. https://doi.org/10.1029/2019jf005058

Johnson, J. P., & Whipple, K. X. (2010). Evaluating the controls of shear stress, sediment supply, alluvial cover, and channel morphology on experimental bedrock incision rate. *Journal of Geophysical Research*, *115*, F02018. https://doi.org/10.1029/2009jf001335

Julien, P. Y., & Anthony, D. J. (2002). Bed load motion and grain sorting in a meandering stream. *Journal of Hydraulic Research*, *40*, 125–133. https://doi.org/10.1080/00221680209499855

Lamb, M. P., Dietrich, W. E., & Sklar, L. S. (2008). A model for fluvial bedrock incision by impacting suspended and bed load sediment. *Journal of Geophysical Research*, *113*, F03025. https://doi.org/10.1029/2007jf000915

Lamb, M. P., Finnegan, N. J., Scheingross, J. S., & Sklar, L. S. (2015). New insights into the mechanics of fluvial bedrock erosion through flume experiments and theory. *Geomorphology*, (Vol. *244*, pp. 33–55). https://doi.org/10.1016/j.geomorph.2015.03.003

Lamb, M. P., & Fonstad, M. A. (2010). Rapid formation of a modern bedrock canyon by a single flood event. *Nature Geoscience*, *3*, 477–481. https://doi.org/10.1038/ngeo894

Langston, A. L., & Tucker, G. E. (2018). Developing and exploring a theory for the lateral erosion of bedrock channels for use in landscape evolution models. *Earth Surface Dynamics*, *6*, 1–27. https://doi.org/10.5194/esurf-6-1-2018

Larsen, I. J., & Montgomery, D. R. (2012). Landslide erosion coupled to tectonics and river incision. *Nature Geoscience*, *5*, 468–473. https://doi.org/10.1038/ngeo1479

Li, T., Fuller, T. K., Sklar, L. S., Gran, K. B., & Venditti, J. G. (2020). A mechanistic model for lateral erosion of bedrock channel banks by bedload particle impacts. *Journal of Geophysical Research: Earth Surface*, *125*, e2019JF005509. https://doi.org/10.1029/2019jf005509

Li, T., Venditti, J. G., & Sklar, L. S. (2021). An analytical model for lateral erosion from saltating bedload particle impacts. *Journal of Geophysical Research: Earth Surface*, *126*, e2020JF006061. https://doi.org/10.1029/2020JF006061

Malatesta, L. C., Prancevic, J. P., & Avouac, J.-P. (2017). Autogenic entrenchment patterns and terraces due to coupling with lateral erosion in incising alluvial channels. *Journal of Geophysical Research: Earth Surface*, *122*, 335–355. https://doi.org/10.1002/2015jf003797

Mishra, J., Inoue, T., Shimizu, Y., Sumner, T., & Nelson, J. M. (2018). Consequences of abrading bed load on vertical and lateral bedrock erosion in a curved experimental channel. *Journal of Geophysical Research: Earth Surface*, *123*, 3147–3161. https://doi.org/10.1029/2017jf004387

Murphy, B. P., Johnson, J. P., Gasparini, N. M., & Sklar, L. S. (2016). Chemical weathering as a mechanism for the climatic control of bedrock river incision. *Nature*, *532*, 223–227. https://doi.org/10.1038/nature17449

Richardson, K., & Carling, P. A. (2005). *A typology of sculpted forms in open bedrock channels* (p. 108.): GSA.

Scheingross, J., Lamb, M. P., & Fuller, B. M. (2019). Self-formed bedrock waterfalls. *Nature*, *567*, 229–233. https://doi.org/10.1038/s41586-019-0991-z

Seizilles, G., Lajeunesse, E., Devauchelle, O., & Bak, M. (2014). Cross-stream diffusion in bedload transport. *Physics of Fluids*, *26*, 013302. https://doi.org/10.1063/1.4861001

Shepherd, R. G. (1972). Incised river meanders: Evolution in simulated bedrock. *Science*, *178*, 409–411. https://doi.org/10.1126/science.178.4059.409

Sklar, L. S., & Dietrich, W. E. (2001). Sediment and rock strength controls on river incision into bedrock. *Geology*, *29*, 1087–1090. https://doi.org/10.1130/0091-7613(2001)029<1087:sarsco>2.0.co;2

Sklar, L. S., & Dietrich, W. E. (2004). A mechanistic model for river incision into bedrock by saltating bed load. *Water Resources Research*, *40*, W06301. https://doi.org/10.1029/2003wr002496

Small, E. E., Blom, T., Hancock, G. S., Hynek, B. M., & Wobus, C. W. (2015). Variability of rock erodibility in bedrock-floored stream channels based on abrasion mill experiments. *Journal of Geophysical Research: Earth Surface*, *120*, 1455–1469. https://doi.org/10.1002/2015jf003506

Timmerman, P., & van der Weele, K. (1999). On the rise and fall of a ball with linear or quadratic drag. *American Journal of Physics*, *67*, 538–546. https://doi.org/10.1119/1.19320

Tsakiris, A. G., Papanicolaou, A. N., & Lauth, T. J. (2014). Signature of bedload particle transport mode in the acoustic signal of a geophone. *Journal of Hydraulic Research*, *52*, 185–204. https://doi.org/10.1080/00221686.2013.876454

Turowski, J. M. (2018). Alluvial cover controlling the width, slope and sinuosity of bedrock channels. *Earth Surface Dynamics*, *6*, 29–48. https://doi.org/10.5194/esurf-6-29-2018

Turowski, J. M. (2020). Mass balance, grade, and adjustment timescales in bedrock channels. *Earth Surface Dynamics*, *8*, 103–122. https://doi.org/10.5194/esurf-8-103-2020

Turowski, J. M., Badoux, A., Leuzinger, J., & Hegglin, R. (2013). Large floods, alluvial overprint, and bedrock erosion. *Earth Surface Processes and Landforms*, *38*, 947–958. https://doi.org/10.1002/esp.3341

Turowski, J. M., Hovius, N., Hsieh, M.-L., Lague, D., & Chiang, M.-C. (2008). Distribution of erosion across bedrock channels. *Earth Surface Processes and Landforms*, *33*, 353–363. https://doi.org/10.1002/esp.1559

Turowski, J. M., & Rickenmann, D. (2009). Tools and cover effects in bedload transport observations in the Pitzbach, Austria. *Earth Surface Processes and Landforms*, *34*, 26–37. https://doi.org/10.1002/esp.1686

Turowski, J. M., Wyss, C. R., & Beer, A. R. (2015). Grain size effects on energy delivery to the streambed and links to bedrock erosion. *Geophysical Research Letters*, *42*, 1775–1780. https://doi.org/10.1002/2015gl063159

Wilson, A., Hovius, N., & Turowski, J. M. (2013). Upstream-facing convex surfaces: Bedrock bedforms produced by fluvial bedload abrasion. *Geomorphology*, *180–181*, 187–204. https://doi.org/10.1016/j.geomorph.2012.10.010